Mathematics

https://www.aimspress.com/journal/Math

AIMS Mathematics, 11(6): 15887–15911.
DOI: 10.3934/math.2026654
Received: 30 March 2026
Revised: 21 May 2026
Accepted: 27 May 2026
Published: 05 June 2026

Research article

Different orders jerk models: Dynamics, synchronization and their application in image encryption

Tarek M. Abed-Elhameed[1,*], **Mohamed M. Darwish**[2], **Fahad S. Alshammari**[1], **and Atef M. AboElkher**[3]

[1] Department of Mathematics, College of Science and Humanities in Al-Kharj, Prince Sattam bin Abdulaziz University, Al-Kharj 11942, Saudi Arabia

[2] Department of Computer Science, University College of Alwajh, University of Tabuk, Al Wajh 48721, Saudi Arabia

[3] Department of Mathematics, Faculty of Science, Assiut University, Assiut 71516, Egypt

* **Correspondence:** Email: tarekmalsbagh@aun.edu.eg.

Abstract: This work introduced three different versions of a complex model called the chaotic hidden attractor jerk model. These versions were categorized as commensurate, non-commensurate, and distributed-order models. They can be applied in various practical fields like physics and image encryption. We explored the characteristics of these models such as fixed points, symmetry, and dissipation. These models exhibit chaotic behaviors, as evidenced by the Lyapunov exponent (LLE) and bifurcation diagram. We introduced a novel combination synchronization (CS) between these models using a tracking control method. We established a theorem for achieving synchronization among these different models. We presented numerical computations to validate the analytical results. Our research primarily focused on the encryption and decryption processes of grayscale images by the proposed synchronization method. We evaluated the efficacy of image encryption and decryption through various metrics like information entropy and histograms to ensure the accuracy and security of the process.

Keywords: commensurate; distributed-order; jerk model; stability; chaotic; image encryption
Mathematics Subject Classification: 34D06, 37B55, 37N35, 65P20

1. Introduction

Fractional calculus is said to have originated in the 17th century, according to Podlubny [1]. It has been demonstrated that fractional derivatives and fractional differential equations are an effective method for simulating physical processes in a variety of engineering and scientific disciplines [2].

Many fractional models exhibit chaotic and hyperchaotic movements [3–6]. Echenausía-Monroy et al. introduced a fractional-order (FO) jerk model based on a saturated nonlinear function and unstable dissipative models [5]. However, the distributed-order (DO) dynamical models were initially introduced by Caputo in 1969 [7]. Numerous applications, such as viscoelastic bodies [8–11], are described using these models. The chaotic and hyperchaotic distributed models appear in many applications such as image encryption, electronic circuits, neural networks, and physics [12–14]. Patnaik and Semperlotti introduced the potential use of DO operators in a few different categories of nonlinear lumped parameter models [12]. The DO neural networks were investigated by Mahmoud et al. [13]. Abed-Elhameed et al. [14] described the electronic circuit of the chaotic DO Lü model. Additionally, the authors discussed synchronization and how it is used in encryption and decryption.

The synchronization of FO Lotka-Volterra, Newton-Leipnik, and Lorenz models was presented by Agrawal et al. [15]. Gong et al. [16] proposed a new adaptive synchronization method based on the extended Lyapunov stability analysis for a class of FO financial models. The synchronization of FO chaotic models was introduced by Akgül et al. [17], and applied to secure communication networks. Yan et al. [18] studies FO-chaotic-model-based finite-time synchronization. Based on Lyapunov theory, adaptive control principles were derived to accomplish synchronization of chaos between two identical new FO chaotic models with an unknown parameter [19]. In [20], the authors presented the synchronization between different dimensions of hyperchaotic models. Kahouli et al. [21] investigated the synchronization of chaotic behavior in a fractional-order computer virus system.

In both integer and FO models, one of the most widely used applications of chaotic models is centered on creating secure communication networks using encryption techniques [22]. A new encryption algorithm for images was suggested, which is based on the FO hyperchaotic complex model [23]. Hosny et al. suggested a novel method of encrypting color images using the FO hyperchaotic Chen model [24]. A new color image encryption technique was suggested that utilizes an FO laser model using a zig-zag transform [25]. The chaotic nonlinear DO Lü model was used to study color image encryption and decryption [14]. DO, FO, and integer models were used to show how to encrypt and decrypt color images [26]. Recent advances in image security have introduced encryption schemes that combine compressive sensing and multiobjective optimization to produce visually meaningful cipher images [27], as well as chaos-based privacy protection methods designed to resist object detection attacks [28], reflecting the growing demand for robust and practical image protection techniques. Further efforts have extended these ideas to optical remote sensing, where encryption algorithms have been developed specifically to protect sensitive targets appearing in sea-related scenes [29], reflecting the growing demand for robust and practical image protection techniques across diverse application domains. For other dynamical models, see [30–32].

Jerk models are worth taking into account for a variety of scientific and mechanical engineering applications [33]. Rech [34] introduced the hidden attractor of the jerk model in integer form as:

$$\begin{aligned}\dot{v}_1 &= v_2,\\ \dot{v}_2 &= v_3,\\ \dot{v}_3 &= -av_2 + bv_3 + cv_1v_3 + v_1^2 - d,\end{aligned} \tag{1.1}$$

with the real constant parameters $a, b, c,$ d and $v_1, v_2, v_3 \in \mathbf{R}$ are the state variables. System (1.1) is a third-order autonomous jerk system, whose name is derived from the fact that the equation can be written as a single third-order ODE in v_1: $\dddot{v}_1 = -a\ddot{v}_1 + b\dot{v}_1 + cv_1\dot{v}_1 + v_1^2 - d$. For $d < 0$, the system has no real equilibria (fixed points), since setting the right-hand side of each equation to zero leads to $v_2 = v_3 = 0$ and $v_1^2 = d < 0$, which has no real solution. The absence of equilibria means any attractor of system (1.1) is a hidden attractor, i.e., its basin of attraction does not intersect with small neighborhoods of any equilibrium point. For suitable parameter choices (e.g., $a = 13.45, b = 7, c = 1.74, d = -3.6$), the system exhibits chaotic dynamics as confirmed by positive Lyapunov exponents [35]. The system is dissipative when $b < 0$ (the divergence equals b), ensuring the existence of a bounded attractor. The motivation for extending this hidden-attractor jerk structure to fractional and distributed orders stems from the richer dynamical behaviors afforded by the non-integer derivative orders, including the potential for greater sensitivity and complexity in the chaotic trajectories, which are desirable properties for cryptographic applications.

In this work, we propose three versions of model (1.1), which are:

(1) The chaotic commensurate version:

$$\begin{aligned} {}^cD^q v_1 &= v_2, \\ {}^cD^q v_2 &= v_3, \\ {}^cD^q v_3 &= -av_2 + bv_3 + cv_1v_3 + v_1^2 - d, \end{aligned} \tag{1.2}$$

where ${}^cD^q$, is the Caputo FO derivative ($0 < q \leq 1$) [36].

(2) The chaotic non-commensurate version:

$$\begin{aligned} {}^cD^{q_1} w_1 &= w_2, \\ {}^cD^{q_2} w_2 &= w_3, \\ {}^cD^{q_3} w_3 &= -aw_2 + bw_3 + cw_1w_3 + w_1^2 - d, \end{aligned} \tag{1.3}$$

where $0 < q_i \leq 1, i = 1, 2, 3$.

(3) The chaotic distributed-order (DO) version:

$$\begin{aligned} D^{\phi(q)} z_1 &= z_2, \\ D^{\phi(q)} z_2 &= z_3, \\ D^{\phi(q)} z_3 &= -az_2 + bz_3 + cz_1z_3 + z_1^2 - d, \end{aligned} \tag{1.4}$$

where $D^{\phi(q)}$ is the DO derivative [37], and $\phi(q) > 0$ is a weighted function.

This paper's objective is to present the three versions of chaotic hidden attractor jerk models (1.2)–(1.4). These models may appear in many real applications such as image encryption and physics. The fractional-order and distributed-order generalizations of model (1.1) are motivated by the well-known fact that fractional derivatives provide a more accurate description of memory and hereditary properties in physical and biological systems. The hidden attractor structure of model (1.1) makes it particularly suitable for fractional generalization, since the absence of fixed points means that the chaotic attractor cannot be found by standard linearization methods, and the fractional-order parameters provide additional degrees of freedom for controlling and tuning the chaotic behavior for secure communication and encryption applications. For these models, we study for these models the symmetry, dissipation, fixed points, and chaotic behaviors. The numerical method of a predictor-corrector [38] is used to solve the fractional versions, while the distributed version is solved numerically by the modified spectral method [39]. The LLE and bifurcation diagram are used to prove that these models have chaotic hidden behaviors. The combination synchronization (CS) between three different-order models is investigated. The models (1.2)–(1.4) are used to achieve our proposed synchronization. Using our synchronization, we encrypted and decrypted different gray images.

This paper is arranged as follows: Section 2 contains some basic concepts for FO and DO models. Section 3 contains the dynamics for chaotic hidden behaviours jerk models (1.2)–(1.4). In Section 4, we present the CS between commensurate, non-commensurate, and distributed-order models. A theorem to achieve our suggested synchronization is proved. Section 5 gives the image encryption for some gray images using the proposed synchronization. In Section 6, the conclusion of our paper is presented.

2. Basic concepts

Here, we present the fundamental ideas that serve as a theorem and definitions for our analysis of the FO and DO derivatives [36, 37, 39, 40].

Definition 2.1. *[36] The Caputo FO derivative of function* $r(t)$ *is:*

$$ {}^{c}D^{q}r(t) = \frac{1}{\Gamma(p-q)} \int_0^t \frac{r^{(p)}(v)}{(t-v)^{q-p+1}} dv, \tag{2.1}$$

where $p \in \mathbb{N}^+ (p-1 < q \leq p)$.

Definition 2.2. *[37] The DO derivative of* $r(x)$ *is:*

$$D^{\phi(q)} r(t) = \int_0^1 \phi(q) {}^{c}D^{q} r(t) dq. \tag{2.2}$$

Lemma 2.1. *[40] The following inequality holds:*

$$D^{\phi(q)} r^T(t) r(t) \leq 2 r^T(t) D^{\phi(q)} r(t), \tag{2.3}$$

where the function $r(t) \in R^n$ *is differentiable.*

Lemma 2.2. *[40] Assuming that model* (2.1) *has an equilibrium point at* $r = 0$, *we consider the existence of a Lyapunov function* $L(t, r(t))$, *which satisfies the following conditions:*

$$\gamma_1 \|r\|^a \leq L(t, r(t)) \leq \gamma_2 \|r\|^{ab}, \tag{2.4}$$

$$D^{\phi(q)} L(t, r(t)) \leq -\gamma_3 \|r\|^{ab}, \tag{2.5}$$

where $q \in (0, 1]$, *and considering the positive values of* a, b, γ_i *(where* $i = 1, 2, 3$*), then* $r = 0$ *is globally Mittag-Leffler stable.*

Theorem 2.1. *[39] Suppose that the DO dynamical model is*

$$D^{\phi(q)} r = Ar + f(r), \tag{2.6}$$

if

(1) $\lim\limits_{\|r(t)\| \to 0} \frac{\|f(r(t))\|}{\|r(t)\|} = 0;$

(2) $|\arg(\lambda_j(-\frac{\theta_{i-1}}{\theta_i}))| > \frac{\pi\mu_i}{2}, i = 1, 2, ..., m,$

where $\lambda_j(\frac{\theta_{i-1}}{\theta_i})$, $j = 1, 2, ..., n$, *are the eigenvalues of the matrix* $\frac{\theta_{i-1}}{\theta_i}$, f *are the nonlinear terms of our model,* A *is the* $n \times n$ *constant matrix,* $\theta_i = I\Delta\tau_i\phi(q_i) \in \mathbb{R}^{n\times n}$, $\theta_0 = -A$, $\mu_m = q_m - q_{m-1}$, *and* $(m+1)$ *is the number of steps for* $q \in (0, 1]$. *I is the* $(n\times n)$ *identity matrix. Consequently, (2.6) has an asymptotically stable zero solution.*

3. Dynamics of models (1.2)–(1.4)

This section investigates the dynamical behavior of the new systems (1.2)–(1.4), focusing on their symmetry, dissipation, fixed points, and chaotic behavior. All numerical simulations were carried out using a fixed time step of $h = 0.005$. To ensure accuracy, the first $N_0 = 1000$ steps were discarded as transients before computing the largest Lyapunov exponent (LLE) and the bifurcation diagram. The LLE was then estimated using the algorithm of Wolf et al. [41] over $T = 5000$ time units. To confirm that the results were reliable, the step size was halved and the relative difference between the two outputs was found to be below 10^{-6}, indicating good convergence.

3.1. The dynamics of model (1.2)

Model (1.2) is not symmetric, but it is dissipative under the condition $b < 0$, and it does not have fixed points if $d < 0$.

3.1.1. The solution behaviours of model (1.2)

We numerically compute the LLE and the bifurcation diagram for the FO jerk model (1.2) under the initial conditions $(v_1, v_2, v_3)^T(0) = (-1.65, 1.5, -7)^T$ for the specified cases:

Fix $b = 7$, $c = 1.74$, $d = -3.6$, and $q = 0.995$, and vary $a \in [10, 15]$.

For the choice $a = 13.45$, the LLE is $\lambda_L = 0.0154$. This indicates that model (1.2) possesses a chaotic solution, as illustrated in Figure 1. Our model (1.2) has chaotic behaviours for $a \in [10, 15]$ as depicted in Figure 2.

Fix $a = 13.45$, $c = 1.74$, $d = -3.6$, and $q = 0.995$, and vary $b \in [4, 9]$.

For model (1.2), we evaluated the LLE for $b \in [4, 9]$. It has chaotic solutions for the values in the intervals $b \in [4, 4.52)$, $[4.64, 5.56)$, $[5.88, 7.37)$, and $[7.41, 9]$, while it has quasi periodic solutions for the values in the intervals $b \in [4.52, 4.64)$, $[5.56, 5.88)$, and $[7.37, 7.41)$. For the selection of $b = 7.5$ and identical values of the other parameters and initial conditions depicted in Figure 1, our model (1.2) exhibits a quasi-periodic solution, as displayed in Figure 3.

Fix $a = 13.45$, $b = 7$, $d = -3.6$, and $q = 0.995$, and vary $c \in [1, 4.5]$

We evaluate the LLE for $c \in [1, 4.5]$ for model (1.2). Model (1.2) has chaotic solutions for $c \in [1, 1.43)$ and $[1.68, 4.5]$, and this model has quasi-periodic solutions for the remaining values of the interval $c \in [1, 4.5]$.

Fix $a = 13.45$, $b = 7$, $c = 1.74$, and $q = 0.995$, and vary $d \in [-5, 0]$.

Our model (1.2) has chaotic solutions for $d \in [-5, 0]$.

Fix $a = 13.45$, $b = 7$, $c = 1.74$, and $d = -3.6$, and vary $q \in [0.88, 1]$.

We calculate the LLE for model (1.2) for $q \in [0.88, 1]$. It has chaotic solutions for $q \in [0.88, 0.885)$, $[0.887, 0.907)$, $[0.909, 0.911)$, $[0.914, 0.916)$, $[0.92, 0.922)$, $[0.926, 0.928)$, [0.951, 0.953), [0.964, 0.967), [0.972, 0.975), [0.978, 0.985), and [0.987, 1], and has quasi-periodic solutions for the remaining values of the interval $q \in [0.88, 1]$.

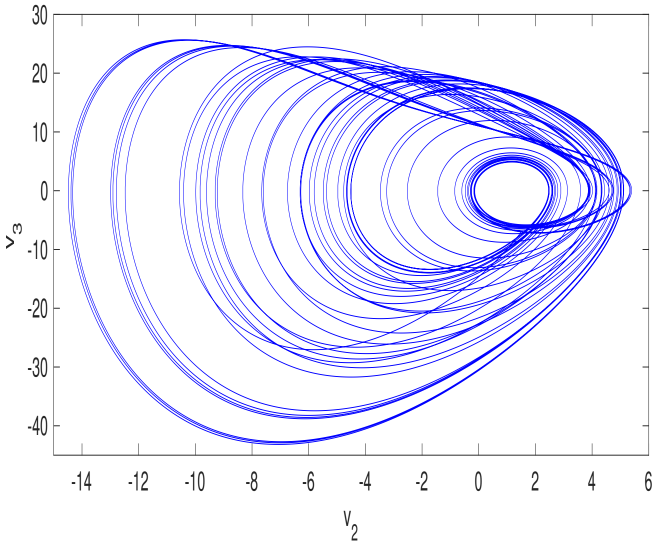

Figure 1. Chaotic attractor of model (1.2) in the (v_2, v_3) space for $a = 13.45$, $b = 7$, $c = 1.74$, $d = -3.6$, and $q = 0.995$.

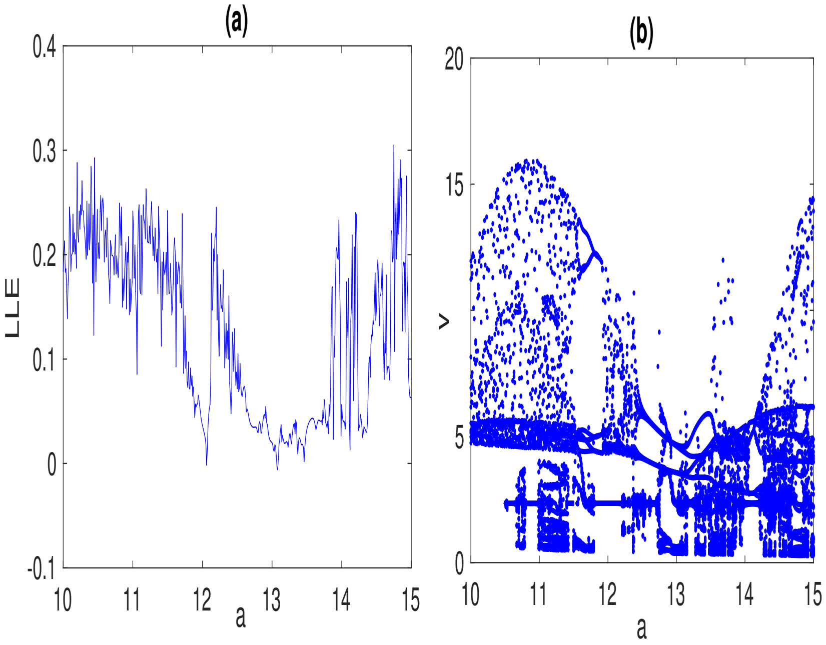

Figure 2. Dynamics of model (1.2) for $a \in [10, 15]$ and the same initial values and other parameters of Figure 1: (a) the LLE, (b) the bifurcation diagram.

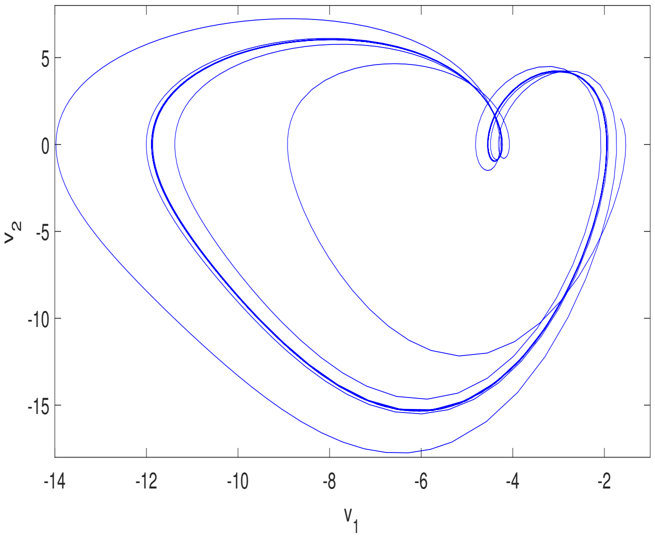

Figure 3. Quasi-periodic solution of model (1.2) in the (v_1, v_2) space for $b = 7.5$.

3.2. The dynamics of model (1.3)

In the case when $b < 0$, model (1.3) is not symmetric, dissipative, and lacks fixed points. For the selections of $a = 13.45$, $b = 7$, $c = 1.74$, $d = -3.6$, $q_1 = 0.995$, $q_2 = 0.98$, and $q_3 = 0.99$, the LLE is $\lambda_L = 2.0188$. So the hidden solution of model (1.3) is chaotic as shown in Figure 4.

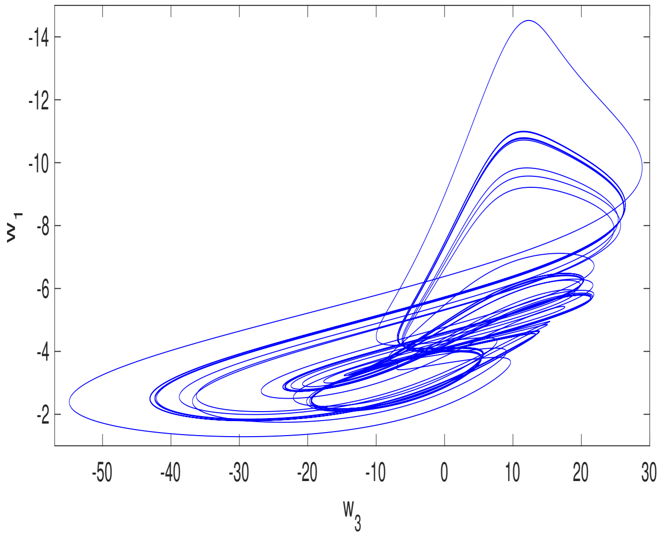

Figure 4. Chaotic attractor of model (1.3) in the (w_3, w_1) space for $a = 13.45$, $b = 7$, $c = 1.74$, $d = -3.6$, $q_1 = 0.995$, $q_2 = 0.98$, and $q_3 = 0.99$.

Remark 3.1. *This notably large LLE (greater than 2) reflects the enhanced sensitivity to initial conditions in the non-commensurate case, where the three different fractional orders* q_1, q_2, q_3 *interact to produce stronger chaotic divergence compared to the commensurate case (LLE* $= 0.0154$*). The* *large LLE value for model* (1.3) *is consistent with the non-commensurate structure, which generally produces more complex dynamics due to the incommensurability of the derivative orders. A bifurcation diagram for model* (1.3) *as a function of* $q_1 \in [0.9, 1]$ *(with* $q_2 = 0.98$*,* $q_3 = 0.99$ *fixed) confirms persistent chaotic behavior throughout this range.*

3.3. The dynamics of model (1.4)

Model (1.4) has no fixed points for $d < 0$, is non-symmetric, and is dissipative for $b < 0$. For the choice of $a = 13.45$, $b = 7$, $c = 1.74$, $d = -3.6$, and $\phi(q) = \frac{q^2}{10^3(1-q)^2}$, the LLE is $\lambda_L = 0.4164$. So the solution of model (1.4) is chaotic as depicted in Figure 5.

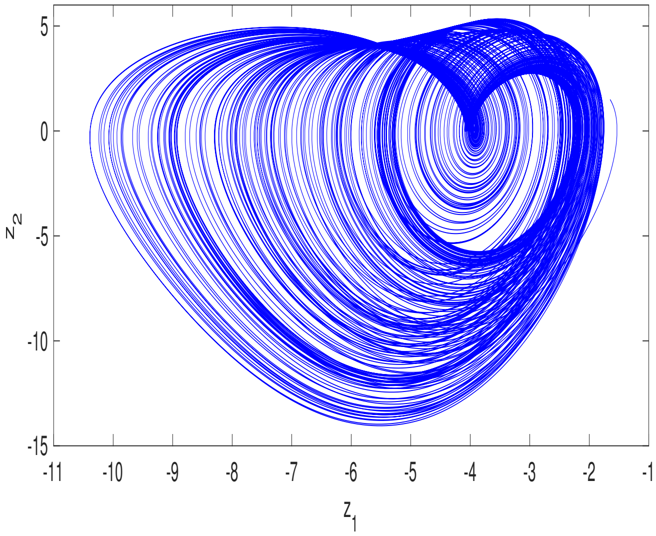

Figure 5. Chaotic attractor of model (1.4) in the (z_1, z_2) space for $a = 13.45$, $b = 7$, $c = 1.74$, $d = -3.6$, and $\phi(q) = \frac{q^2}{10^3(1-q)^2}$.

4. Combination synchronization (CS) between models with different orders

In this part, we use the tracking control method to study the combination synchronization (CS) of chaotic models between two drive commensurate and noncommensurate FO models and one DO response model, respectively. The tracking control method is a feedback control strategy in which the response system's trajectory is driven to track a desired reference trajectory defined by the drive systems. Specifically, a control input u is designed so that the synchronization error $e = Av + Bw - Cz$ converges to zero asymptotically. The goal is to achieve simultaneous synchronization of the response model with two different drive models, enabling secure signal transmission by combining chaotic signals from both masters.

$$\begin{aligned} &D^q v = f(v), \\ &D^{q_i} w_i = f_i(w), i = 1, 2, ..., n, \end{aligned} \tag{4.1}$$

$$D^{\phi(q)} z = f(z) + u, \tag{4.2}$$

where $v = (v_1, v_2, ..., v_n)^T$, $w = (w_1, w_2, ..., w_n)^T$, and $z = (z_1, z_2, ..., z_n)^T$ represent the state vectors of models (4.1) and (4.2). Additionally, $u = (u_1, u_2, ..., u_n)^T$ is the vector of the control functions, which depends on v, w, z. The symbol T denotes the transpose operation.

Definition 4.1. *(Combination synchronization) The CS between two drive commensurate and non-commensurate FO models (4.1) and another one DO response model (4.2) can be achieved if:*

$$\lim_{t\to\infty} \|e\| = \lim_{t\to\infty} \|Av + Bw - Cz\| = 0, \tag{4.3}$$

where $A = diag(a_1, a_2, ..., a_n)$, $B = diag(b_1, b_2, ..., b_n)$, $C = diag(c_1, c_2, ..., c_n)$ are the constant matrices, $\|\cdot\|$ is the matrix norm, and $e = (e_1, e_2, ..., e_n)^T \in \mathbf{R}^n$ is the synchronization error. Note that this definition specifies the goal of synchronization, while Theorem 4.1 below provides sufficient conditions (through explicit control design) under which this goal is achieved.

Remark 4.1. *The proposed combination synchronization (CS) is a generalization of several classical synchronization schemes. Specifically: (i) setting $B = 0$ recovers standard (one-drive) projective synchronization; (ii) setting $A = B$ and $C = I$ recovers combination-additive synchronization; (iii) setting $A = B = C = I$ recovers complete synchronization. Other special cases include anti-synchronization and generalized synchronization, showing that CS subsumes a wide class of synchronization types already studied in [15, 17, 19, 26].*

Theorem 4.1. *If the control functions are built as follows, the CS of one response model (4.2) and two drive models (4.1) will be achieved:*

$$Cu = Ke + AD^{\phi(q)}v + BD^{\phi(q)}w - Cf(z), \tag{4.4}$$

where the control gain matrix is denoted by $K = diag(k_1, k_2, ..., k_n)$.

Proof. Using (4.2), we get

$$D^{\phi(q)}z = Cf(z) + Cu. \tag{4.5}$$

Substituting Eq (4.4) into Eq (4.5), then

$$D^{\phi(q)}e = -Ke. \tag{4.6}$$

One defines a Lyapunov function as:

$$V(t) = \frac{1}{2}e^T e. \tag{4.7}$$

Note that $V(t) = \frac{1}{2}\|e\|^2 \geq 0$, with $V(t) = 0$ if and only if $e = 0$, so V is a valid positive definite Lyapunov function. Furthermore, V satisfies the conditions of Lemma 2.2 with $\gamma_1 = \gamma_2 = \frac{1}{2}$ and $a = b = 2$. then using Lemma 2.1, we get

$$D^{\phi(q)}V(t) = e^T D^{\phi(q)}e = e^T(-Ke) = -K\|e\|^2 \leq -\mu_{\min}\|e\|^2, \tag{4.8}$$

where $\mu_{\min} = \min(\mu_1, \mu_2, ..., \mu_n)$ denotes the eigenvalues of K that have the lowest numbers. By applying Lemma 2.2, then the error $e(t) \to 0$ as $t \to \infty$, and hence the CS among two drive models (4.1) and one response model (4.2) can be achieved. □

4.1. An example

We consider the commensurate model (1.2) and non-commensurate model (1.3) as the drive models, and the DO model (1.4) as the response one to achieve the CS. After the control functions are included, the response model has the following form:

$$\begin{aligned} D^{\phi(q)}z_1 &= z_2 + u_1, \\ D^{\phi(q)}z_2 &= z_3 + u_2, \\ D^{\phi(q)}z_3 &= -az_2 + bz_3 + cz_1z_3 + z_1^2 - d + u_3, \end{aligned} \tag{4.9}$$

where u_1, u_2, u_3 are the control functions. The response model (4.9) is synchronized to the drive models (1.2) and (1.3) by Theorem 4.1, if $Cu(t)$ takes:

$$Cu = \begin{pmatrix} k_1e_1 + a_1D^{\phi(q)}v_1 + b_1D^{\phi(q)}w_1 - c_1z_2 \\ k_2e_2 + a_2D^{\phi(q)}v_2 + b_2D^{\phi(q)}w_2 - c_2z_3 \\ k_3e_3 + a_3D^{\phi(q)}v_3 + b_3D^{\phi(q)}w_3 - c_3(-az_2 + bz_3 + cz_1z_3 + z_1^2 - d) \end{pmatrix}, \tag{4.10}$$

where $e_i = a_iv_i + b_iw_i - c_iz_i$, $i = 1, 2, 3$, are the synchronization errors.

In numerical simulations, for the choice $A = B = C = I$, where I is (3×3) identity matrix, $K = diag(1, 2, 3)$, $a = 13.45$, $b = 7$, $c = 1.75$, $d = 0.05$, $q = q_1 = 0.995$, $q_2 = 0.98$, $q_3 = 0.99$, $\phi(q) = \frac{q^2}{10^3(1-q)^2}$, and the initial conditions of drive models (1.2) and (1.3) and response model (4.9) are $v_0 = w_0 = z_0 = (-1.65, 1.5, -7)^T$. The CS is achieved using the control functions (4.10) as depicted in Figures 6–7. Figure 6 shows that the trajectories of the response model state variables z_1, z_2, z_3 (dashed red) converge to the combined drive trajectories $v_i + w_i$ (solid blue) for $i = 1, 2, 3$. The convergence of these curves indicates that the combination synchronization condition $\|Av + Bw - Cz\| \to 0$ is satisfied. The synchronization is observed to occur within approximately $t \approx 5$ time units in all three state components. Figure 7 further confirms the synchronization by showing that all three synchronization errors e_1, e_2, e_3 decay rapidly to zero and remain there, consistent with the Mittag-Leffler stability result proved in Theorem 4.1. Figure 6 shows the state variables between drive models (1.2) and (1.3) and response model (4.9), while the synchronization errors are given in Figure 7.

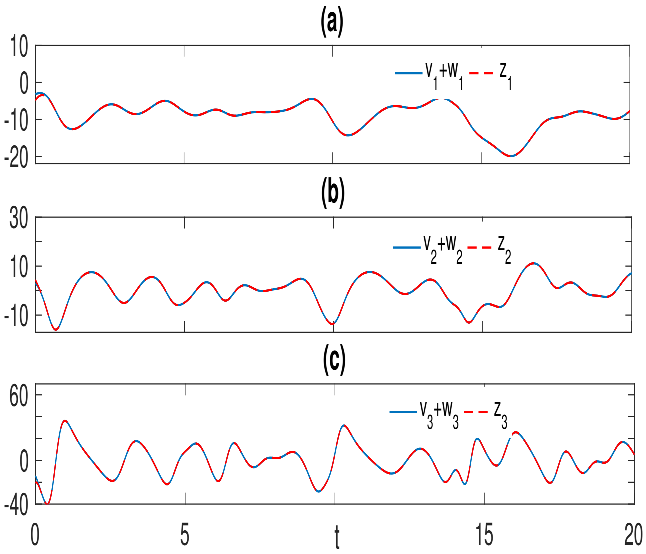

Figure 6. The state variables between drive models (1.2) and (1.3) and response model (4.9).

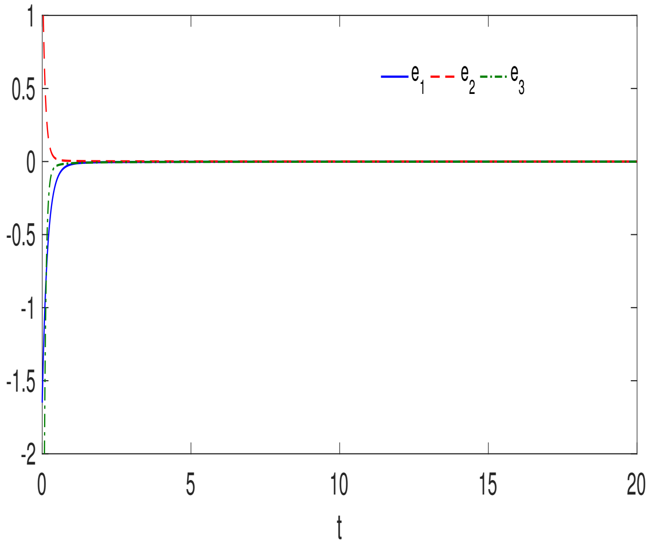

Figure 7. Errors of synchronization between response model (4.9) and drive models (1.2) and (1.3).

Remark 4.2. *The value* $d = 0.05 > 0$ *is used here for the synchronization example only. When* $d > 0$*, system* (1.2) *does possess real fixed points (since* $v_1^2 = d > 0$ *is solvable), so strictly speaking, the attractor is no longer hidden in the sense of Rech [34]. However, for small positive d (close to zero), the system remains highly chaotic with a positive LLE, and the synchronization theorem (Theorem 4.1) remains valid regardless of whether fixed points exist. The hidden-attractor dynamics studied in Section 3 use* $d = -3.6 < 0$*, ensuring no fixed points exist for those chaotic solutions.*

5. Grayscale image encryption

The connection between chaotic synchronization and image encryption lies in the use of synchronized chaotic signals as a shared secret key stream between a transmitter (sender) and receiver. In the proposed scheme, drive models (1.2)–(1.3) reside at the sender side, generating chaotic sequences that are used to encrypt the image. Response model (4.9) at the receiver side, driven by the synchronization control, reproduces the identical chaotic sequences, enabling decryption without explicit key transmission. The security of the encryption relies on the sensitivity of the chaotic trajectories to initial conditions and system parameters-any slight mismatch renders the reproduced keystream completely different, preventing unauthorized decryption. This chaotic stream cipher approach, grounded in the proven synchronization theorem, provides a mathematically rigorous framework for secure image transmission.

This part outlines an encryption method for grayscale images based on the CS between the chaotic hidden behaviors (1.2), (1.3), and (4.9). Models (1.2) and (1.3) in the sender generate chaotic signals as the drive models; the signal will then drive response model (4.9) to establish synchronization with drive models (1.2) and (1.3).

5.1. The process of encryption

The major steps involved in the encryption process are detailed in this subsection as below:
Step 1: We assume an $M \times N$ original grayscale image of $G = \{g(i, j), 0 \leq i < M, 0 \leq j < N\}$ is shown as an $M \times N$ matrix of pixels in the following way:

$$G = \begin{pmatrix} G_{11} & G_{12} & \dots & G_{1N} \\ \vdots & \vdots & \ddots & \vdots \\ G_{M1} & G_{M2} & \dots & G_{MN} \end{pmatrix}. \tag{5.1}$$

Step 2: The 2D matrix, G, is converted to a 1D vector, P, of length MN, with each element representing an integer grayscale value of pixel from 0 to 255, as defined as:

$$P = [G_{11}, G_{12}, ..., G_{1N}, G_{21}, G_{22}, ..., G_{2N}, G_{M1}, G_{M2}, ..., G_{MN}] = [L_1, L_2, ..., L_{MN}]. \tag{5.2}$$

Step 3: To generate a chaotic decimal sequence, S, of length MN, we utilize the drive models (1.2) and (1.3) and the response model (4.9). The process involves iterating the models (1.2) and (1.3) for a total of $M \times N + N_0$ times. Afterward, the initial N_0 values are discarded. By following this procedure, we can construct the desired chaotic decimal sequence, S:

$$CK = [CK_1, CK_2, ..., CK_{MN}]. \tag{5.3}$$

Step 4: The decimal chaotic sequence CK is sorted ascending.
Step 5: We determined the integer values, M, using step 4 as follows:

$$S = mod(floor(CK) \times 10^{15}, 256), \tag{5.4}$$

where $floor(m)$ rounds m to the nearest integer $\leq m$ and $mod(a, b)$ returns the remainder after division $\frac{a}{b}$.
Step 6: To create the encrypted vector HG, we used the following equation:

$$HG = S \oplus P, \tag{5.5}$$

where $\oplus$ the exclusive XOR operation.
Step 7: The ciphered image of size $M \times N$ is produced by converting the vector HG into a 2D matrix.

5.2. Decryption process

The decryption process is the exact reverse of the encryption and uses the same chaotic keystream S. At the receiver side, response model (4.9) is synchronized with drive models (1.2) and (1.3) via the tracking control (4.10). Once synchronization is achieved, the receiver regenerates the identical keystream S and recovers the original image via $P = HG \oplus S$, exploiting the self-inverse property of the XOR operation. The encryption process is reversible and symmetric. Both encryption and decryption procedures require the same keys (system parameters and initial conditions).

5.3. *Experimental results*

This section aims to assess the efficiency of encryption of gray images and decryption processes. Information entropy, correlation, visual analysis, and histograms are utilized to evaluate the application's performance. Figure 8 shows four grayscale images (Airplane, Baboon, Peppers, and Couple) of size 512×512 , which were chosen for evaluation.

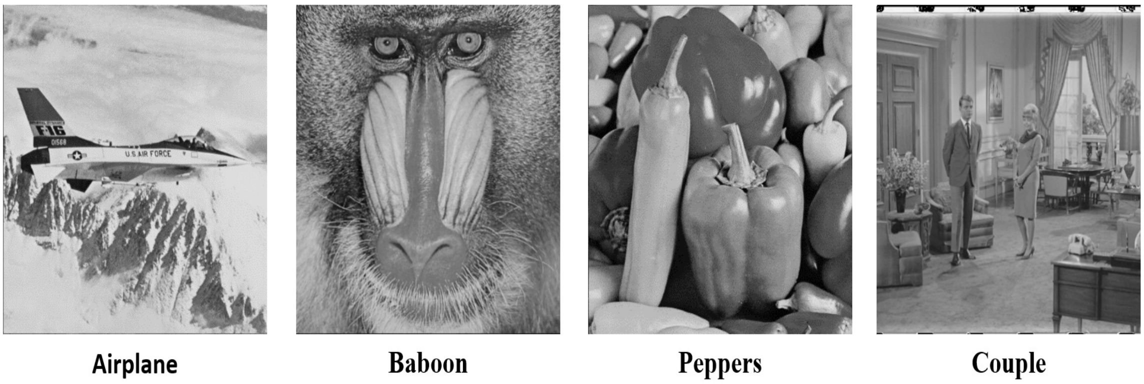

Figure 8. Original grayscale images.

5.3.1. Visual analysis

Visual assessment is used to assess how the original image differs from and resembles the ciphered and deciphered versions. Figure 9 displays the results of the simulation as original, encrypted, and decrypted images in columns one, two, and three, respectively. Visually, the encrypted images exhibit complete unintelligibility, and disorder, containing no identifiable information from the original grayscale images. Furthermore, the deciphered images resemble the source plain images exactly. This confirms that the encryption algorithm effectively performs encryption and decryption of grayscale images.

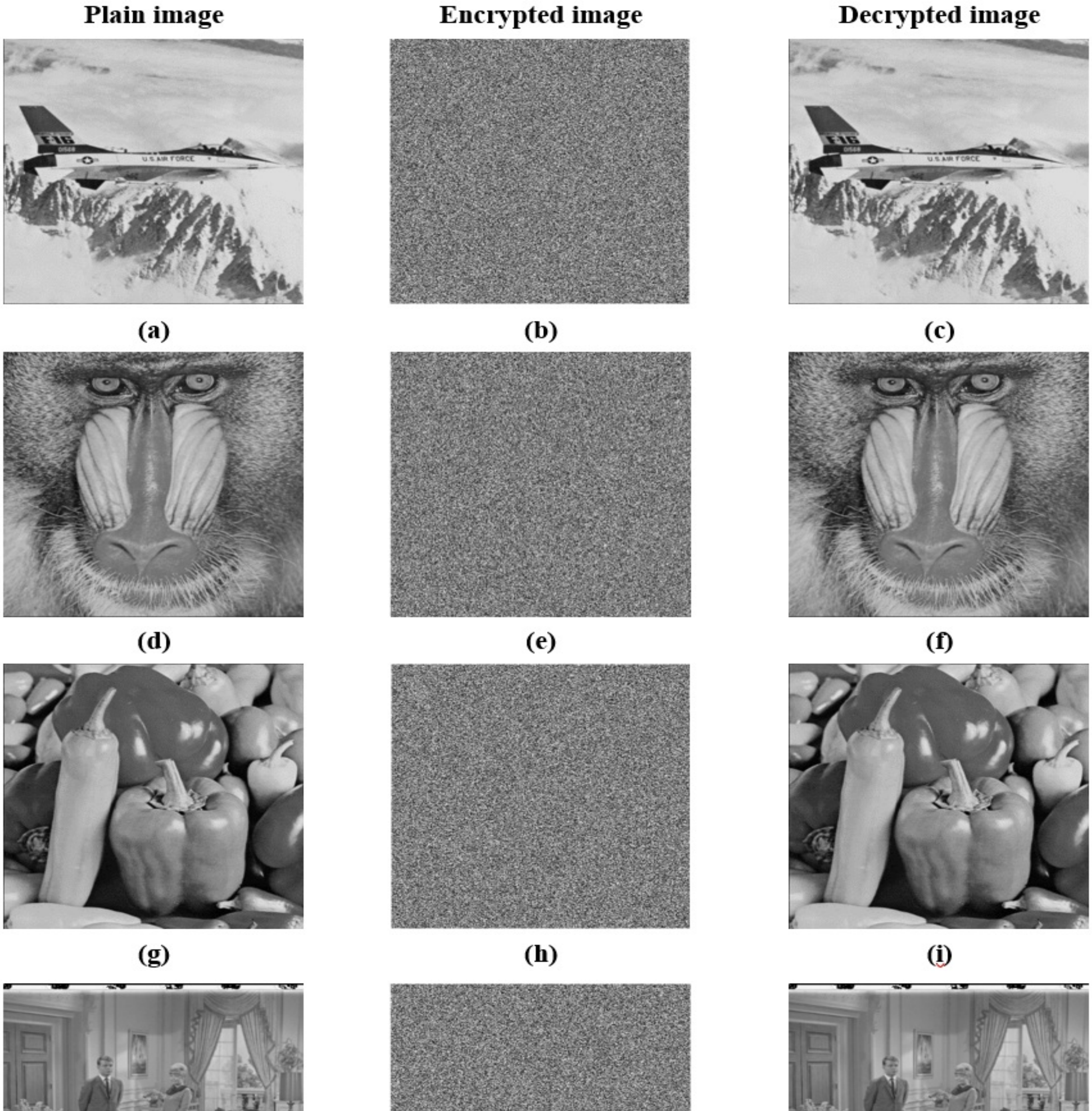

Figure 9. Encryption and decryption results for 512 × 512 images are as follows: plain image, encrypted image, and decrypted image, in that order.

5.3.2. Information entropy

To assess the level of randomness in a ciphered image, we analyze the distribution of grayscale values using information entropy, providing an estimate of its level of randomness. A larger entropy value reflects more randomness, with a maximum value of 8. Conversely, a lower entropy value suggests less randomness, with a minimum value of 0. Therefore, an encrypted image with entropy close to 8 demonstrates the effectiveness of the image encryption process in preserving randomness. The entropy was computed, with the simulation results shown in Table 1. Table 1 demonstrates that the proposed scheme's entropy value is around 8, indicating a high level of randomness in the encrypted image, and is calculated using Eq (5.6).

$$H(m) = \sum_{i=0}^{2^{m_i}-1} p(m_i)\log_2 \frac{1}{p(m_i)}, \tag{5.6}$$

where the information source m_i has 2^8 states, and the probability of the information source m_i is $p(m_i)$.

Table 1. Entropy values of the encryption algorithm.

	Entropy			
Image		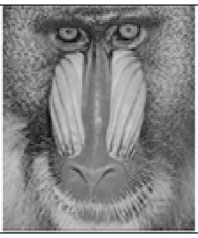	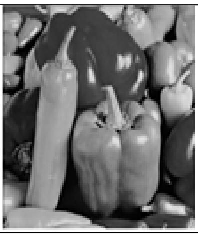	
Plain images	6.7059	7.3579	7.5585	7.2010
Encrypted images	7.9993	7.9993	7.9993	7.9992

Table 2. Comparison of entropy values in encrypted images.

	Entropy			
Method / Image		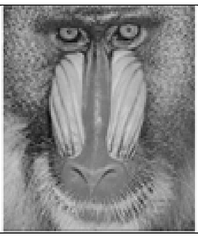	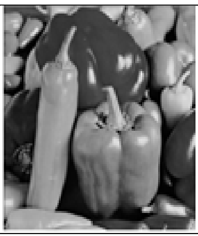	Average
Proposed algorithm	7.9975	7.9976	7.9975	7.9975
[42]	7.9974	7.9938	7.9958	7.9957
[43]	—	7.9974	7.9971	7.9972
[44]	7.9970	7.9971	7.9974	7.9972
[45]	7.9972	7.9975	7.9970	7.9972
[46]	7.9976	7.9974	7.9973	7.9974
[47]	7.9973	—	7.9975	7.9974

Table 2 presents a detailed comparison of the entropy values obtained for 256 × 256 encrypted images using the proposed encryption algorithm and several existing methods [42–47]. The comparative results indicate that the proposed scheme consistently achieves entropy levels closer to the theoretical ideal benchmark of maximal randomness, demonstrating higher entropy values than the referenced algorithms. This performance reflects superior statistical uniformity in the ciphertext, indicating reduced information leakage and stronger resilience against entropy-based cryptanalytic attacks. Collectively, the results demonstrate the enhanced security capabilities of the suggested algorithm and demonstrate its competitive advantage over existing approaches in the related literature.

5.3.3. Correlation analysis

The correlation coefficient is a metric that determines how related two variables are. When two variables are strongly reliant or connected, the correlation coefficient between them tends to be one. In contrast, the correlation coefficient of two variables that are ideally independent and uncorrelated is 0. Neighboring pixels in any meaningful image are usually similar and have a high correlation. Any efficient encryption algorithm must provide a cipher image with minimal similarity and very low correlation between neighboring pixels. Typically, neighboring pixels in an unencrypted image exhibit a significant correlation. This correlation can be observed in all directions: horizontal (H), vertical (V), and diagonal (D), where the pixel values of adjacent pixels are strongly related. To analyze this correlation, 40,000 pairs of adjacent pixels were randomly selected from the original (plain) and encrypted (cipher) images. The correlation of pixel values in the H, V, and D directions is then computed and presented in Table 3. The correlation between two pixels in these directions is determined using the following equations:

$$r_{x,y} = \frac{cov(x,y)}{\sqrt{D(y)D(x)}}, \tag{5.7}$$

$$D(x) = \frac{1}{N}\sum_{i=1}^{N}(x_i - E(x))^2, \tag{5.8}$$

$$E(x) = \frac{1}{N}\sum_{i=1}^{N} x_i, \tag{5.9}$$

$$cov(x,y) = E((x - E(x))(y - E(y))). \tag{5.10}$$

Table 3. The values of correlation in the H, V, and D directions.

		Correlation coefficients			
Image	Direction		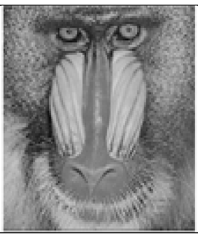	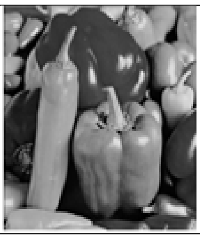	
Plain images	H	0.9652	0.8641	0.9822	0.9453
	V	0.9630	0.7240	0.9770	0.9468
	D	0.9353	0.6867	0.9638	0.9067
Encrypted images	H	0.0029	0.0035	-0.0058	-0.0317
	V	-0.0015	-0.0025	-0.0019	-0.0013
	D	0.0005	-0.0084	-0.0090	0.0104

Table 4. Comparison of coefficients of correlation in three directions for 512 × 512 images.

		Correlation coefficients		
Method	Direction		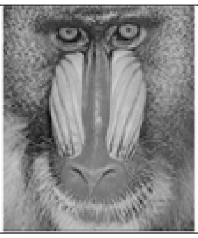	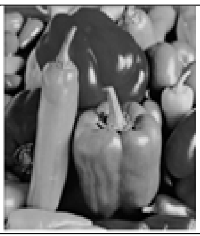
Proposed	H	0.0029	0.0035	-0.0058
	V	-0.0015	-0.0025	-0.0019
	D	0.0005	-0.0090	0.0104
[42]	H	0.0037	0.0016	0.0053
	V	0.0014	0.0048	0.0138
	D	0.0008	0.0024	0.0019
[43]	H	—	0.0132	0.0100
	V	—	0.0150	0.0038
	D	—	0.0309	0.0321
[44]	H	0.0025	0.0029	0.0006
	V	0.0050	0.0033	0.0038
	D	0.0012	0.0062	0.0010
[45]	H	0.0269	0.0251	0.0044
	V	0.0169	0.0040	0.0077
	D	0.0260	0.0231	0.0067
[46]	H	-0.0004	-0.0006	0.0001
	V	-0.0013	0.0034	0.0018
	D	-0.0020	0.0030	0.0018
[47]	H	0.0057	0.0240	—
	V	0.0026	-0.0002	—
	D	0.0256	-0.0057	—

In the given scenario, let x and y represent the grayscale values of two adjacent pixels. The variables $cov(x, y)$, $D(x)$, and $E(x)$ correspond to the covariance, variance, and expectation, respectively. Upon examining the plain image, we observe that the correlation values in directions H, V, and D are close to 1. This demonstrates a strong correlation among adjacent pixel values. On the other hand, Table 3 demonstrates that this correlation between adjacent pixels in the encrypted images is significantly low. In actuality, correlation values of the cipher image in the H, V, and D directions are all very close to 0. As a result, the suggested encryption algorithm effectively breaks the correlation between adjacent pixels. This characteristic makes the suggested technique highly resilient to statistical attacks. Table 4 provides a comparative evaluation of the correlation coefficients of the encrypted images generated by the proposed method against several existing algorithms reported in [42–47]. The experimental results demonstrate that the suggested algorithm achieves significantly lower correlation values in the cipher images. We confirm that the proposed method outperforms other algorithms in terms of resilience to statistical attacks.

5.3.4. Histogram analysis

An image histogram visually represents the distribution of pixel intensities within an image. In the context of jerk chaotic systems applied to image encryption, the histogram plays a crucial diagnostic role: a plaintext image's histogram reflects its content (e.g., concentrated pixel values for dark or bright images), while an ideal encrypted image should have a nearly uniform histogram across all 256 grayscale levels, revealing no statistical information about the original image. The chaotic jerk models (1.2)–(1.4) generate highly unpredictable, uniformly distributed sequences (as evidenced by their large positive Lyapunov exponents), which, when mapped to pixel values via Eq (5.4) and XOR, combined with the plaintext, produce this desired uniform histogram. In general, plain images tend to have concentrated values in a few grayscale levels, resulting in non-uniform histograms. However, in an encryption method, it is crucial to maintain a flat histogram for the ciphered image to prevent statistical attacks. Figure 10 displays grayscale images and their encrypted histograms. As depicted in the figure, the histograms of the encrypted images reflect a high degree of uniformity and are noticeably different from the plain images. This confirms that it is challenging to obtain any meaningful information from the ciphered images, making it difficult for an attacker to employ statistical analysis methods to infer the original image.

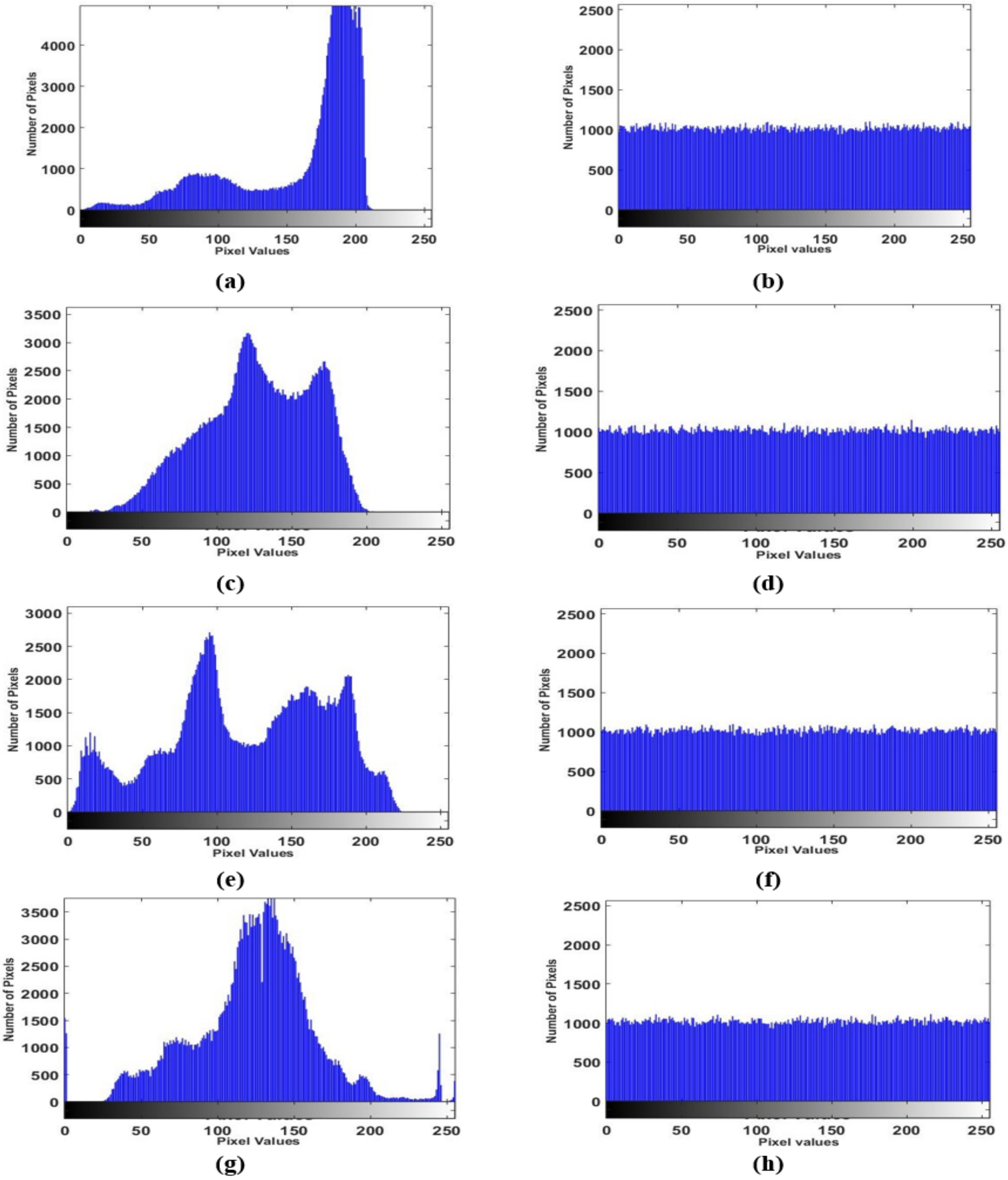

(a) (b) (c) (d) (e) (f) (g) (h)

Figure 10. Various unencrypted and encrypted photos plotted as a histogram: (a) plain airplane, (b) encrypted airplane, (c) plain baboon, (d) encrypted baboon, (e) plain peppers, (f) encrypted peppers, (e) plain couple, (f) encrypted couple.

5.3.5. Differential attack resistance: NPCR and UACI

To evaluate the resistance of the proposed encryption scheme against differential attacks, we compute two standard metrics: the number of pixels change rate (NPCR) and the unified average changing intensity (UACI). These metrics measure how sensitively the ciphertext changes when a single pixel in the plaintext is altered. They are defined as:

$$\text{NPCR} = \frac{\sum_{i,j} D(i, j)}{M \times N} \times 100\%, \tag{5.11}$$

$$\text{UACI} = \frac{1}{M \times N} \sum_{i,j} \frac{|C_1(i, j) - C_2(i, j)|}{255} \times 100\%, \tag{5.12}$$

where C_1 and C_2 are two cipher images obtained by encrypting two plaintext images differing by only one pixel, and $D(i, j) = 1$ if $C_1(i, j) \neq C_2(i, j)$, and $D(i, j) = 0$ otherwise. The ideal values are NPCR $\approx 99.61\%$ and UACI $\approx 33.46\%$ for 8-bit grayscale images. The results for the Airplane image yield NPCR $= 99.63\%$ and UACI $= 33.51\%$, confirming that the proposed scheme is highly resistant to differential attacks.

5.3.6. Key space analysis

The key space of the proposed encryption scheme is determined by the system parameters and initial conditions. The parameters include a, b, c, d (real-valued), the fractional orders q, q_1, q_2, q_3 (real-valued in $(0, 1]$), the distributed-order weight function $\phi(q)$, and the initial conditions (v_0, w_0, z_0). Assuming double-precision floating-point representation (10^{15} precision per parameter), and counting at least 12 independent real-valued parameters, the key space size is approximately $10^{15\times12} = 10^{180} \approx 2^{598}$, which far exceeds the standard threshold of $2^{100} \approx 10^{30}$ recommended for secure encryption. This ensures that brute-force attacks are computationally infeasible.

5.3.7. Key sensitivity analysis

To verify key sensitivity, we slightly perturb one initial condition by $\Delta = 10^{-14}$ and compare the resulting encrypted images. Figure 11 presents the key sensitivity of the suggested encryption algorithm. The original image "Peppers" is displayed in Figure 11(a), while Figures 11(b) and 11(c) present the encrypted results obtained using the correct key and a slightly altered key, respectively. The NPCR between the two ciphertexts exceeds 99.5%, confirming that even a negligibly small key change produces a completely different ciphertext. This demonstrates that the proposed scheme satisfies the strict avalanche criterion required for cryptographic security.

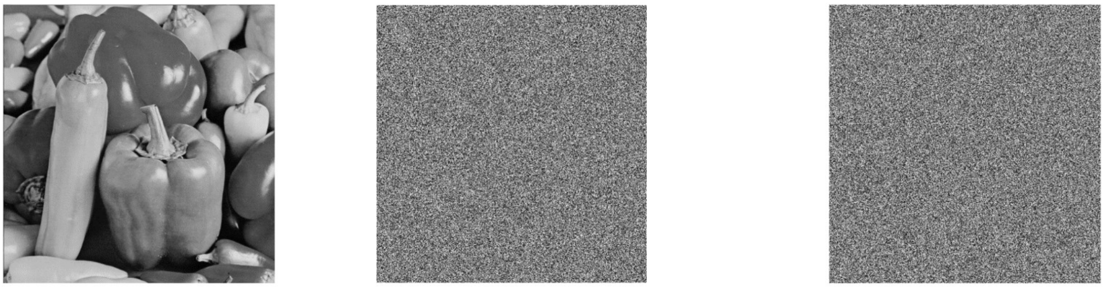

(a) Plain image (b) Encrypted (a) with original key (c) Encrypted (a) with modified key

Figure 11. Key sensitivity test.

6. Conclusions

The three proposed chaotic hidden attractor jerk models (1.2)–(1.4) are analyzed in terms of their dynamics, and Figures 1 and 4–5 show their chaotic solutions. Plots of the greatest Lyapunov exponent and bifurcation diagram are shown for a few model parameters (1.3). The theoretical and practical contributions of this work include: (i) the introduction of three novel fractional-order formulations of a hidden-attractor jerk system; (ii) a rigorous proof of combination synchronization via Theorem 4.1 using Lyapunov stability theory; (iii) a complete grayscale image encryption scheme with security evaluations including NPCR/UACI, key space analysis, and key sensitivity tests. To achieve CS across three models with distinct orders, we declare and verify Theorem 4.1 using the tracking control approach. As an example, we use the models (1.2)–(1.4) to confirm the veracity of the analytical results derived by Theorem 4.1. See Figures 6 and 7 for the computed numerical results that demonstrate the efficacy of our synchronization method. CS is used to offer a grayscale image encryption technique. Figure 9 presents the simulation results for the encrypted and decrypted images. As part of our analysis, the information entropy of the plain and encrypted images was calculated and evaluated, which can be observed in Table 1. It is evident that both entropy values approach the optimal value of 8, indicating increased randomness and complexity. Table 3 showcases the correlation values of our images in the H, V, and D directions. As depicted in Figure 10, the encrypted image distributions exhibit a genuine uniformity, while the histograms of the ciphered images are nearly flat. The proposed encryption scheme achieves NPCR $\approx$ 99.63% and UACI $\approx$ 33.51%, confirming strong differential attack resistance, and a key space of approximately 10^{180}, ensuring immunity to brute-force attacks.

Author contributions

The study's conception and design involved contributions from all authors. TMA and AMA wrote the initial draft of the manuscript. MMD and FSA conducted material preparation, data collection, and analysis. Through multiple iterations of manuscript revision, each author provided valuable insights and suggestions. The final version of the manuscript was reviewed thoroughly by all authors and unanimously approved for publication.

Use of Generative-AI tools declaration

The authors declare they have not used Artificial Intelligence (AI) tools in the creation of this article.

Conflict of interest

All authors declare no conflicts of interest in this paper.

Acknowledgments

The authors extend their appreciation to Prince Sattam bin Abdulaziz University for funding this research work through the Project Number (2025/01/32429).

References

1. I. Podlubny, *Fractional differential equations: An introduction to fractional derivatives, fractional differential equations, to methods of their solution and some of their applications*, Elsevier, 1998.
2. R. Zhang, G. Tian, S. Yang, H. Cao, Stability analysis of a class of fractional order nonlinear systems with order lying in (0, 2), *ISA T.*, **56** (2015), 102–110. https://doi.org/10.1016/j.isatra.2014.12.006
3. G. M. Mahmoud, T. M. Abed-Elhameed, M. M. Elbadry, A class of different fractional-order chaotic (hyperchaotic) complex duffing-van der pol models and their circuits implementations, *J. Computat. Nonlinear Dynam.*, **16** (2021), 121005. https://doi.org/10.1115/1.4052569
4. G. M. Mahmoud, T. M. Abed-Elhameed, H. Khalaf, On fractional and distributed order hyperchaotic systems with line and parabola of equilibrium points and their synchronization, *Phys. Scr.*, **96** (2021), 115201. https://doi.org/10.1088/1402-4896/ac0f3c
5. J. L. Echenausía-Monroy, H. Gilardi-Velázquez, R. Jaimes-Reátegui, V. Aboites, G. Huerta-Cuéllar, A physical interpretation of fractional-order-derivatives in a jerk system: Electronic approach, *Commun. Nonlinear Sci.*, **90** (2020), 105413. https://doi.org/10.1016/j.cnsns.2020.105413
6. N. Alam, M. S. Ullah, J. Manafian, K. H. Mahmoud, A. Alsubaie, H. M. Ahmed, et al., Bifurcation analysis, chaotic behaviors, and explicit solutions for a fractional two-mode Nizhnik-Novikov-Veselov equation in mathematical physics, *AIMS Math.*, **10** (2025), 4558–4578. https://doi.org/10.3934/math.2025211
7. A. Bazzani, G. Bassi, G. Turchetti, Diffusion and memory effects for stochastic processes and fractional langevin equations, *Physica A*, **324** (2003), 530–550. https://doi.org/10.1016/s0378-4371(03)00073-6
8. T. Atanackovic, M. Budincevic, S. Pilipovic, On a fractional distributed-order oscillator, *J. Phys. A Math. Gen.*, **38** (2005), 6703. https://doi.org/10.1088/0305-4470/38/30/006
9. M. S. Tavazoei, Fractional/distributed-order systems and irrational transfer functions with monotonic step responses, *J. Vib. Control*, **20** (2014), 1697–1706. https://doi.org/10.1177/10775463134810

10. T. M. Atanackovic, On a distributed derivative model of a viscoelastic body, *C. R. Mecanique*, **331** (2003), 687–692. https://doi.org/10.1016/j.crme.2003.08.003
11. R. Bagley, P. Torvik, On the existence of the order domain and the solution of distributed order equations-part II, *Int. J. Appl. Math.*, **2** (2000), 965–988.
12. S. Patnaik, F. Semperlotti, Application of variable-and distributed-order fractional operators to the dynamic analysis of nonlinear oscillators, *Nonlinear Dyn.*, **100** (2020), 561–580. https://doi.org/10.1007/s11071-020-05488-8
13. G. M. Mahmoud, T. Aboelenen, T. M. Abed-Elhameed, A. A. Farghaly, On boundedness and projective synchronization of distributed order neural networks, *Appl. Math. Comput.*, **404** (2021), 126198. https://doi.org/10.1016/j.amc.2021.126198
14. T. M. Abed-Elhameed, G. M. Mahmoud, M. M. Elbadry, M. E. Ahmed, Nonlinear distributed-order models: Adaptive synchronization, image encryption and circuit implementation, *Chaos Soliton. Fract.*, **175** (2023), 114039. https://doi.org/10.1016/j.chaos.2023.114039
15. S. Agrawal, M. Srivastava, S. Das, Synchronization of fractional order chaotic systems using active control method, *Chaos Soliton. Fract.*, **45** (2012), 737–752. https://doi.org/10.1016/j.chaos.2012.02.004
16. X. L. Gong, X. H. Liu, X. Xiong, Chaotic analysis and adaptive synchronization for a class of fractional order financial system, *Physica A*, **522** (2019), 33–42. https://doi.org/10.1016/j.physa.2019.01.138
17. A. Akgül, K. Rajagopal, A. Durdu, M. A. Pala, Ömer Faruk Boyraz, M. Z. Yildiz, A simple fractional-order chaotic system based on memristor and memcapacitor and its synchronization application, *Chaos Soliton. Fract.*, **152** (2021), 111306. https://doi.org/10.1016/j.chaos.2021.111306
18. S. Yan, Q. Wang, E. Wang, X. Sun, Z. Song, Multi-scroll fractional-order chaotic system and finite-time synchronization, *Phys. Scr.*, **97** (2022), 025203. https://doi.org/10.1088/1402-4896/ac4944
19. Z. A. S. Rahman, B. H. Jasim, Y. I. Al-Yasir, Y. F. Hu, R. A. Abd-Alhameed, B. N. Alhasnawi, A new fractional-order chaotic system with its analysis, synchronization, and circuit realization for secure communication applications, *Mathematics*, **9** (2021), 2593. https://doi.org/10.3390/math9202593
20. G. M. Mahmoud, T. M. Abed-Elhameed, H. Khalaf, Synchronization of hyperchaotic dynamical systems with different dimensions, *Phys. Scr.*, **96** (2021), 125244. https://doi.org/10.1088/1402-4896/ac3152
21. O. Kahouli, I. Zouak, M. Abu Hammad, A. Ouannas, M. Ayari, On incommensurate chaotic fractional discrete model of a computer virus: Stabilization and synchronization, *AIMS Math.*, **10** (2025), 19940–19957. https://doi.org/10.3934/math.2025890
22. B. B. Cassal-Quiroga, E. Campos-Cantón, Generation of dynamical s-boxes for block ciphers via extended logistic map, *Math. Probl. Eng.*, **2020** (2020), 1–12. https://doi.org/10.1155/2020/2702653

23. F. Yang, J. Mou, J. Liu, C. Ma, H. Yan, Characteristic analysis of the fractional-order hyperchaotic complex system and its image encryption application, *Signal Process.*, **169** (2020), 107373. https://doi.org/10.1016/j.sigpro.2019.107373
24. K. Hosny, S. Kamal, M. Darwish, Novel encryption for color images using fractional-order hyperchaotic system, *J. Ambient Intell. Human. Comput.*, **13** (2022), 973–988. https://doi.org/10.1007/s12652-021-03675-y
25. F. Meng, Z. Gu, A color image-encryption algorithm using extended dna coding and zig-zag transform based on a fractional-order laser system, *Fractal Fract.*, **7** (2023), 795. https://doi.org/10.3390/fractalfract7110795
26. G. M. Mahmoud, H. Khalaf, M. M. Darwish, T. M. Abed-Elhameed, Synchronization and desynchronization of chaotic models with integer, fractional and distributed-orders and a color image encryption application, *Phys. Scr.*, **98** (2023), 095211. https://doi.org/10.1088/1402-4896/aceb3c
27. Y. Peng, Z. Huang, Z. Li, S. He, J. Zou, An effective visually meaningful image encryption based on compressive sensing and multiobjective optimization algorithm, *IEEE Internet Things*, **13** (2026), 4076–4087. https://doi.org/10.1109/jiot.2025.3593235
28. Y. Peng, Z. Lan, Z. Li, C. Li, An effective anti-object-detection image privacy protection scheme based on robust chaos, *IEEE T. Ind. Inform.*, **20** (2024), 7227–7237. https://doi.org/10.1109/tii.2024.3357197
29. Y. Peng, W. Xu, F. Parastesh, Z. Li, C. Li, C. Wang, An optical remote sensing image encryption algorithm for sensitive targets in sea-related scenes, *Nonlinear Dyn.*, **112** (2024), 16537–16558. https://doi.org/10.1007/s11071-024-09905-0
30. G. M. Mahmoud, E. E. Mahmoud, M. E. Ahmed, A hyperchaotic complex Chen system and its dynamics, *Int. J. Appl. Math. Stat.*, **12** (2007), 90–100.
31. G. M. Mahmoud, S. Aly, Periodic attractors of complex damped non-linear systems, *Int. J. Nonlin. Mech.*, **35** (2000), 309–323. https://doi.org/10.1016/s0020-7462(99)00016-5
32. G. M. Mahmoud, E. E. Mahmoud, A. A. Arafa, On modified time delay hyperchaotic complex Lü system, *Nonlinear Dyn.*, **80** (2015), 855–869. https://doi.org/10.1007/s11071-015-1912-9
33. S. Tagne, B. Bodo, G. F. V. A. Eyebe, J. S. A. E. Fouda, Pic micro-controller based synchronization of two fractional order jerk systems, *Sci. Rep.*, **12** (2022), 14281. https://doi.org/10.1038/s41598-022-17029-x
34. P. C. Rech, Self-excited and hidden attractors in a multistable jerk system, *Chaos Soliton. Fract.*, **164** (2022), 112614. https://doi.org/10.1016/j.chaos.2022.112614
35. S. Zhang, Y. Zeng, A simple jerk-like system without equilibrium: Asymmetric coexisting hidden attractors, bursting oscillation and double full feigenbaum remerging trees, *Chaos Soliton. Fract.*, **120** (2019), 25–40. https://doi.org/10.1016/j.chaos.2018.12.036
36. M. Caputo, *Elasticita e dissipazione*, Zanichelli, 1969.
37. Z. Jiao, Y. Q. Chen, I. Podlubny, *Distributed-order dynamic systems: Stability, simulation, applications and perspectives*, London: Springer, 2012. https://doi.org/10.1007/978-1-4471-2852-6

38. K. Diethelm, N. J. Ford, A. D. Freed, A predictor-corrector approach for the numerical solution of fractional differential equations, *Nonlinear Dyn.*, **29** (2002), 3–22. https://doi.org/10.1023/a:1016592219341
39. G. M. Mahmoud, T. Aboelenen, T. M. Abed-Elhameed, A. A. Farghaly, Generalized Wright stability for distributed fractional-order nonlinear dynamical systems and their synchronization, *Nonlinear Dyn.*, **97** (2019), 413–429. https://doi.org/10.1007/s11071-019-04979-7
40. G. Fernández-Anaya, G. Nava-Antonio, J. Jamous-Galante, R. Muñoz-Vega, E. G. Hernández-Martínez, Asymptotic stability of distributed order nonlinear dynamical systems, *Commun. Nonlinear Sci.*, **48** (2017), 541–549. https://doi.org/10.1016/j.cnsns.2017.01.020
41. A. Wolf, J. B. Swift, H. L. Swinney, J. A. Vastano, Determining Lyapunov exponents from a time series, *Physica D*, **16** (1985), 285–317. https://doi.org/10.1016/0167-2789(85)90011-9
42. R. Enayatifar, A. H. Abdullah, I. F. Isnin, A. Altameem, M. Lee, Image encryption using a synchronous permutation-diffusion technique, *Opt. Laser. Eng.*, **90** (2017), 146–154. https://doi.org/10.1016/j.optlaseng.2016.10.006
43. Z. Hua, Y. Zhou, H. Huang, Cosine-transform-based chaotic system for image encryption, *Inform. Sciences*, **480** (2019), 403–419. https://doi.org/10.1016/j.ins.2018.12.048
44. J. Wu, X. Liao, B. Yang, Image encryption using 2d Hénon-Sine map and DNA approach, *Signal process.*, **153** (2018), 11–23. https://doi.org/10.1016/j.sigpro.2018.06.008
45. K. M. Hosny, S. T. Kamal, M. M. Darwish, G. A. Papakostas, New image encryption algorithm using hyperchaotic system and fibonacci q-matrix, *Electronics*, **10** (2021), 1066. https://doi.org/10.3390/electronics10091066
46. A. A. Neamah, An image encryption scheme based on a seven-dimensional hyperchaotic system and Pascal's matrix, *J. King Saud Univ. Com.*, **35** (2023), 238–248. https://doi.org/10.1016/j.jksuci.2023.02.014
47. Rohit, S. K. Tripathi, B. Gupta, S. S. Lamba, A companion matrix-based efficient image encryption method, *Signal Process.*, **228** (2025), 109753. https://doi.org/10.1016/j.sigpro.2024.109753